



HAL
open science

Polycrystalline simulations of in-reactor deformation of zircaloy-4 cladding tubes during nominal operating conditions

Cécilia Gicquel, Fabien Onimus, Renald Brenner, Thomas Helfer, Renaud Masson

► To cite this version:

Cécilia Gicquel, Fabien Onimus, Renald Brenner, Thomas Helfer, Renaud Masson. Polycrystalline simulations of in-reactor deformation of zircaloy-4 cladding tubes during nominal operating conditions. Zirconium in the Nuclear Industry: 20th International Symposium, ASTM STP 1645, ASTM International, pp.118-148, inPress, 10.1520/STP164520220048 . hal-04318054

HAL Id: hal-04318054

<https://hal.science/hal-04318054>

Submitted on 1 Dec 2023

HAL is a multi-disciplinary open access archive for the deposit and dissemination of scientific research documents, whether they are published or not. The documents may come from teaching and research institutions in France or abroad, or from public or private research centers.

L'archive ouverte pluridisciplinaire **HAL**, est destinée au dépôt et à la diffusion de documents scientifiques de niveau recherche, publiés ou non, émanant des établissements d'enseignement et de recherche français ou étrangers, des laboratoires publics ou privés.

C. Gicquel, F. Onimus, R. Brenner, T. Helfer, R. Masson (2022). Polycrystalline simulations of in-reactor deformation of Zircaloy-4 cladding tubes during nominal operating conditions. 20th International Symposium on Zirconium in the Nuclear Industry, ASTM STP 1645, Eds. S. Yagnik & M. Preuss, ASTM International, West Conshohocken, pp. 118-148, doi: 10.1520/STP164520220048.

Polycrystalline simulations of in-reactor deformation of Zircaloy-4 cladding tubes during nominal operating conditions

Cécilia Gicquel^{1,2}, Fabien Onimus^{1,*}, Renald Brenner², Thomas Helfer³, Renaud Masson³

¹Université Paris-Saclay, CEA, Service de Recherches Métallurgiques Appliquées, Gif-sur-Yvette, France.

²Institut Jean le Rond d'Alembert, Sorbonne Université, 4 place Jussieu, CC162, 75252 Paris Cedex 05, France

³CEA, DES, IRESNE, DEC, Cadarache F-13108 Saint-Paul-Lez-Durance, France

*Corresponding author: fabien.onimus@cea.fr

Abstract:

Fuel cladding tubes, made of zirconium alloys are subjected, in-reactor, to a complex loading history under nominal operating conditions. Furthermore, they exhibit a complex deformation behavior resulting from irradiation induced growth, irradiation creep and thermal creep. For design and safety requirements, empirical models are usually used. To have robust physically based mechanical simulations, a self-consistent polycrystalline model has been developed. This model takes into account the various phenomena occurring at the grain scale, such as irradiation induced growth and irradiation creep. Moreover, this model takes into account the crystallographic texture of the material and the mechanical interactions between grains, depending on their orientation. Furthermore, this model is able to handle complex mechanical loading. This model is first shown to reproduce well an experimental database of in-reactor deformation of zirconium alloys. Thanks to the polycrystalline nature of this model, the effect of grain shape and creep mechanisms at the grain scale on the simulated data have been studied in detail. Next, this polycrystalline model has been introduced into a 1D Finite Element Method code, allowing the computation of stress and strain gradients through a thin cladding tube during a complex mechanical loading. This approach opens the way to physically based mechanical calculations at the component scale.

Keywords— homogenization, polycrystal, creep, growth, self-consistent

1. Introduction

Zirconium alloys are used in the nuclear industry as fuel rod cladding tubes in pressurized water reactors. During nominal operating conditions, the cladding experiences simultaneous neutron irradiation and complex biaxial loading history¹. First, the cladding tube exhibits a creep down towards the pellet due to the pressure of the primary water that is only partially balanced by the internal pressure inside the fuel rod. After an initial phase of densification, the pellet swells. Then, when the pellet and the cladding are in contact, the pellet swelling leads to the biaxial straining of the cladding tube. These complex deformations must be well characterized and predicted for safe and efficient in-reactor operation. The in-reactor deformation of zirconium alloy cladding tubes is the result of three different phenomena: thermal creep, irradiation creep and irradiation induced growth^{2,3}. Thermal creep is the usual creep occurring even in the absence of irradiation and is often considered negligible during in-reactor deformation under low applied stress. Irradiation creep is a specific deformation phenomenon that occurs under an applied stress and is activated by the fast neutron flux⁴. Irradiation induced growth is a special deformation phenomenon because it occurs under fast neutron flux without any applied stress^{5,6}. Several authors^{7,8} have proposed empirical macroscopic models to account for the in-reactor deformation of zirconium alloys. In those models, the polycrystalline nature of the material is not taken into account. However, it was early recognized⁹ that the polycrystalline character of the material and the interactions between grains can play a significant role on the macroscopic behavior. This work has been followed by the development of several self-consistent polycrystalline models. One can distinguish the models aiming to estimate only the steady-state creep response^{10,11} and the models aiming to also describe the transient response resulting from the coupling between elasticity and (nonlinear) viscosity^{12,13,14}. The latter essentially rely on hereditary integral approaches using Laplace-Carson transforms.

During the past several years, a renewed interest in the modelling of in-reactor deformation of zirconium alloys has arisen with the development of multiscale approaches from the single crystal to the structure component that couples a viscoplastic self-consistent model with a finite element code^{15,16}. Recently, full-field simulations, based on the Fast Fourier Transform method, have also been applied to the in-reactor behavior of recrystallized Zircaloy-4 guide tubes¹⁷. Despite the large body of work done on this subject during the past 30 years, the influence of a complex loading history on the in-reactor polycrystalline response of the material has not yet been evaluated in detail.

In the present work, we propose to implement a polycrystalline non-ageing linear viscoelastic (*i.e.* elastic and irreversible viscous behavior) self-consistent model with an internal variables formulation¹⁸. This approach offers a convenient framework to describe the mechanical response for a complex loading history of aging nonlinear viscoelastic materials^{19,20}. Following early works^{10,12,13,21}, the local behavior of the crystalline grains is chosen as empirical without considering explicitly the detailed deformation mechanisms. However, the physics of the mechanical interactions between grains is taken into account as accurately as possible. This model has been implemented in the MFront code

generation tool²² allowing a straightforward coupling with finite element codes for structure computation. This model has been applied to the in-reactor behavior of cold-work stress relieved and recrystallized Zircaloy-4 thin tubes.

This approach provides for the first time a self-consistent polycrystalline model able to describe the transient resulting from the visco-elastic coupling at the local scale and a model able to handle complex loading history such as changing the stress or strain state. This model also allows a straightforward coupling with finite element computation at the component scale.

First, the two materials and the mechanical tests are described. Then, the principle of the polycrystalline model is presented and the parameter fitting procedure is described. Finally, the simulation results are shown and discussed.

Eventually, in the last section, the polycrystalline model is coupled with a 1D finite element code and its response to a complex loading history, mimicking the in-reactor nominal condition, is described.

2. Materials and mechanical test data base

The two materials studied in this work are made of a zirconium alloy called Zircaloy-4 and noted Zy-4. Its chemical content, given in weight % is the following: 1.30% Sn, 0.21% Fe, 0.10-0.12%Cr, 0.125-0.128%O.

This alloy is studied in two different metallurgical states: the cold-worked stress-relieved metallurgical state, also referred to as stress relief annealed (SRA), and the recrystallized metallurgical state, referred to as recrystallization annealed (RXA). These two materials differ due to the last heat treatment conducted after the last cold working step. The SRA alloy has been heat treated at temperatures around 475°C and the RXA alloy has been heat treated at temperatures²³ in the range of 530 to 600°C. The resulting microstructure of these two materials is very different.

The SRA alloy exhibits long elongated grains, with a length of about 20 µm along the rolling direction, which corresponds to the axial direction of the tube, and a typical width of 2 µm along the two other directions. These elongated grains are further subdivided by low angle boundaries into smaller cells, typically 0.2 µm wide. This alloy also contains a high dislocation density, especially $\langle a \rangle$ dislocations but also many $\langle c+a \rangle$ dislocations.

Concerning the RXA material, the grains are equiaxed²⁴ with a typical size of 5 µm. The grains contain very few dislocations, only some $\langle a \rangle$ dislocations but no $\langle c+a \rangle$ dislocations.

These two material exhibit similar crystallographic textures^{23,25}. The $\langle c \rangle$ axis of the grains is tilted 30-40° away from the radial direction of the tube, toward the hoop direction (circumferential). After cold-rolling the $\langle 10\bar{1}0 \rangle$ direction is parallel to the rolling direction, and the $\langle 1\bar{2}10 \rangle$ direction is being tilted about 30° from the z-axis. During the

recrystallization heat treatment, a 30° rotation occurs around the <c>-direction, and the rolling direction is then aligned with the $\langle \bar{1}2\bar{1}0 \rangle$ direction for most of the grains.

In the following, the z direction corresponds to the axial direction of the tube, the y direction corresponds to the hoop or circumferential direction of the tube (often referred to as θ) and the x direction corresponds to the radial direction of the tube (often referred to as r).

The in-reactor behavior of these two materials has been studied by Gilbon et al.²⁶, and Soniak et al.²⁷. These authors conducted irradiation creep tests at 350°C under internal pressure in the CEA material testing reactors Siloé and Osiris using pre-pressurized cladding tube specimens. Furthermore, stress free samples have also been irradiated in the same conditions to measure the irradiation induced growth strain. To obtain the target hoop stress, the tubes were pressurized with an internal pressure (P) such that at irradiation temperature, the hoop stress is given by the following approximated formula²⁸ Eq. 1.

$$\sigma_{yy} \approx \frac{PD_m^{ini}}{2e} \quad (1)$$

In Eq. 1 e is the initial cladding thickness and D_m^{ini} is the initial mean diameter given by $D_m^{ini} = D_{ext}^{ini} - e$, with ($D_{ext}^{ini}=9.5$ mm and $e=0.6$ mm).

Because of the closed end of the tube, an axial stress also arises that is approximately equal to half the hoop stress ($\sigma_{zz} \approx \sigma_{yy}/2$). The creep tests have been conducted on SRA Zy-4 using three different hoop stresses (60, 90 and 120 MPa) and on RXA Zy-4 using two hoop stresses (90 and 120 MPa). From the database provided in this work, all the tests conducted at 350°C under a fast neutron flux ($E > 1$ MeV) close to 1.7×10^{18} n.m⁻².s⁻¹ have been selected. In the following, a mean flux of 1.7×10^{18} n.m⁻².s⁻¹ is considered for all the experiments. Because the hoop strain remains small during the test, the change of internal pressure is considered to remain negligible. The initial external diameter ($D_{ext}(0)$) and length ($L(0)$) are measured before irradiation at room temperature and under an applied stress, and the diameter ($D_{ext}(t)$) and length ($L(t)$) of the samples are regularly measured at room temperature and under an applied stress, in a hot cell, for both creep and growth samples, by taking the samples out of the reactor. From these measurements, the mean axial and hoop creep strain or growth strain are computed using the formula Eq. 2 and Eq. 3, where $D_m(0) = D_{ext}(0) - e$.

$$\epsilon_{yy}^m = \ln \left(1 + \frac{D_{ext}(t) - D_{ext}(0)}{D_m(0)} \right) \quad (2)$$

$$\epsilon_{zz}^m = \ln \left(1 + \frac{L(t) - L(0)}{L(0)} \right) \quad (3)$$

3. Description of the self-consistent polycrystalline model

An estimation of the linear viscoelastic response of the polycrystal is derived on the basis of the use of the correspondence principle together with the self-consistent model. We take advantage of the internal variables formulation proposed by Ricaud and Masson^{18,19} to implement this homogenization model for textured 3D polycrystals in the MFront code generation tool²². This allows a straightforward coupling with a finite-element code to describe the mechanical response of fuel cladding tubes during nominal operating conditions.

3.1 Local problem

Let us consider a polycrystalline material with volume Ω containing grains with N different crystalline orientations (g). The set of all grains with the same orientation represents the constitutive phase (g) occupying the volume Ω_g with volume fractions c_g . The polycrystal is subjected to homogeneous conditions of stress $\bar{\sigma}(t)$ or strain histories $\bar{\varepsilon}(t)$ on the outer boundary $\partial\Omega$. The time-dependent stress and strain fields are thus solutions to the following local problem described in Eq. 4.

$$\begin{aligned} \operatorname{div}\sigma(x, t) &= 0, \quad \operatorname{curl} \left({}^T \operatorname{curl}(\varepsilon(x, t)) \right) = 0, \quad \forall x \in \Omega \\ \varepsilon(x, t) &= \int_0^t \mathbf{M}^{(g)}(t-u) : \dot{\sigma}(x, u) du + \varepsilon_0^{(g)}(t), \quad \forall x \in \Omega_g \quad (g = 1, \dots, N) \\ \bar{\sigma}(t) &= \langle \sigma(x, t) \rangle, \quad \bar{\varepsilon}(t) = \langle \varepsilon(x, t) \rangle \end{aligned} \quad (4)$$

$\langle \cdot \rangle$ denotes the average over the volume Ω . $\mathbf{M}^{(g)}(t)$ and $\varepsilon_0^{(g)}(t)$ represent respectively the local viscoelastic compliance tensor and the stress-free strain which are uniform within each constitutive phase (g). The local behavior is assumed to be Maxwellian, meaning that it follows Eq. 5.

$$\mathbf{M}^{(g)}(t) = \mathbf{M}_e^{(g)} + t\mathbf{M}_v^{(g)} \quad (5)$$

where $\mathbf{M}_e^{(g)}$ and $\mathbf{M}_v^{(g)}$ the elastic and viscous compliance tensors respectively.

The assumption of a linear dependence of irradiation creep with stress can be justified by considering that the rate controlling process of irradiation creep deformation is the point defect diffusion towards dislocations or grain boundaries.

In addition, the stress-free strain $\varepsilon_0^{(g)}(t)$ describes the irradiation growth of each phase.

The local strain rate $\dot{\varepsilon}(x, t)$ can be expressed as Eq. 6.

$$\begin{aligned}\dot{\varepsilon}(x, t) &= \dot{\varepsilon}^e(x, t) + \dot{\varepsilon}^v(x, t) + \dot{\varepsilon}_0^{(g)}(t) \\ &= \mathbf{M}_e^{(g)} : \dot{\sigma}(x, t) + \mathbf{M}_v^{(g)} : \sigma(x, t) + \dot{\varepsilon}_0^{(g)}(t), \quad \forall x \in \Omega_g\end{aligned}\quad (6)$$

Note that, except for the irradiation growth, the strain rates vary within each phase (g). It must also be pointed out that this constitutive equation (Eq. 6) assumes uncoupled creep and growth deformation processes. This is probably not true considering that both processes result from point defect diffusion and dislocation climb. However, the results given by Gharbi et al.²⁹ suggest a very limited effect of an applied stress on breakaway growth thus partly justifying our uncoupled approach.

3.2 Overall behaviour and phase-averaged fields

The polycrystal is subjected to loading time functions consisting of the overall stress $\bar{\sigma}(t)$ and the prescribed growth strains $\varepsilon_0^{(g)}(t)$ which are continuous functions of time (*i.e* no time discontinuities). The overall constitutive law can be expressed as a Stieltjes convolution product (Eq. 7).

$$\bar{\varepsilon}(t) = \int_0^t \tilde{\mathbf{M}}(t-u) : \dot{\bar{\sigma}}(u) du + \tilde{\varepsilon}_0(t) \quad (7)$$

where $\tilde{\mathbf{M}}(t)$ the effective creep function and $\tilde{\varepsilon}_0(t)$ the time evolution of the overall irradiation growth strain. The latter is given by equation 8.

$$\tilde{\varepsilon}_0(t) = \sum_{g=1}^N c_g \int_0^t {}^T \mathbf{B}^{(g)}(t-u) : \dot{\varepsilon}_0^{(g)}(u) du \quad (8)$$

where $\mathbf{B}^{(g)}(t)$ represent the time evolution of the stress localization tensor averaged over phase (g) with volume fraction c_g .

In addition, the phase-averaged stress $\sigma_g(t)$ and strain $\varepsilon_g(t)$ fulfill the following interaction law (Eq. 9).

$$\varepsilon_g(t) - \bar{\varepsilon}(t) = - \int_0^t \mathbf{T}(t-u) : (\dot{\sigma}_g(u) - \dot{\bar{\sigma}}(u)) du \quad (9)$$

where \mathbf{T} is the interaction tensor defined in equation 10.

3.3 Internal variables formulation

The self-consistent estimate of the macroscopic behaviour and the average local fields is derived by approximating the tensors $\tilde{\mathbf{M}}(t)$, $\mathbf{B}^{(g)}(t)$ and $\mathbf{T}(t)$ by Dirichlet series expansions as follows (Eq. 10):

$$\begin{aligned} \tilde{\mathbf{M}}(t) &\approx \tilde{\mathbf{M}}_e + t\tilde{\mathbf{M}}_v + \sum_{i=1}^{N_c} \tilde{\mathbf{M}}_i \left(1 - e^{-\frac{t}{\tau_i}}\right) \\ \mathbf{T}(t) &\approx \mathbf{T}_e + t\mathbf{T}_v + \sum_{i=1}^{N_c} \mathbf{T}_i \left(1 - e^{-\frac{t}{\tau_i}}\right) \\ \mathbf{B}^{(g)}(t) &\approx \mathbf{B}_e^{(g)} + \sum_{i=1}^{N_c} \mathbf{B}_i^{(g)} \left(1 - e^{-\frac{t}{\tau_i}}\right), \quad (g = 1, \dots, N) \end{aligned} \quad (10)$$

The tensors $(\tilde{\mathbf{M}}_e, \mathbf{T}_e, \mathbf{B}_e^{(g)})$ and $(\tilde{\mathbf{M}}_v, \mathbf{T}_v)$ are respectively obtained from the self-consistent estimate for the purely elastic and viscous heterogeneous problems. The unknown tensors $\mathbf{M}_i, \mathbf{T}_i$ and $\mathbf{B}_i^{(g)}$ are classically determined by the collocation method which makes use of the correspondence principle³⁰. It requires arbitrarily to choose N_c collocation times τ_i . In this work, we chose five collocation times distributed on a logarithmic scale between 1×10^6 s and 1×10^9 s. Following Ricaud and Masson¹⁸, an internal variables formulation of the overall constitutive law Eq. 7 and the interaction law Eq. 9 is obtained by incorporating the approximations Eq. 10 into the hereditary integral relations. The effective constitutive law now reads (Eq. 11):

$$\bar{\varepsilon}(t) = \tilde{\mathbf{M}}_e : \bar{\sigma}(t) + \underbrace{\xi(t) + \sum_{i=1}^{N_c} \zeta_i(t)}_{\tilde{\varepsilon}^v(t)} + \underbrace{\sum_{g=1}^N c_g \left[\mathbf{B}_e^{(g)} : \varepsilon_0^{(g)}(t) + \sum_{i=1}^{N_c} \eta_i^{(g)}(t) \right]}_{\tilde{\varepsilon}_0(t)} \quad (11)$$

where $\tilde{\varepsilon}^v(t)$ denotes the time evolution of the macroscopic viscous strain. $\xi(t)$ represents its steady-state part while the sum $\sum_i \zeta_i(t)$ is the contribution of the transient regime. The effective growth strain $\tilde{\varepsilon}_0(t)$ contains an elastic part and a contribution of the viscoelastic coupling with the sums $\sum_i \eta_i^{(g)}(t)$, $\forall g = 1, \dots, N$. The evolution equations of these internal variables are given by equation 12.

$$\begin{aligned} \dot{\xi}(t) &= \tilde{\mathbf{M}}_v : \bar{\sigma}(t), \quad \xi(0) = 0, \\ \tau_i \dot{\zeta}_i(t) + \zeta_i(t) &= \tilde{\mathbf{M}}_i : \bar{\sigma}(t), \quad \forall i \in [1; N_c], \quad \zeta_i(0) = 0, \\ \tau_i \dot{\eta}_i^{(g)}(t) + \eta_i^{(g)}(t) &= \mathbf{B}_i^{(g)} : \varepsilon_0^{(g)}(t), \quad i \in [1; N_c], \quad \forall g \in [1; N], \quad \eta_i^{(g)}(0) = 0 \end{aligned} \quad (12)$$

The interaction law can also be written as Eq. 13.

$$\varepsilon_g(t) - \bar{\varepsilon}(t) = -\mathbf{T}_e : (\sigma_g(t) - \bar{\sigma}(t)) - \beta_g(t) - \sum_{i=1}^{N_c} \gamma_i^{(g)}(t) \quad (13)$$

with the following evolution equations defining the internal variables $\beta_g(t)$ and $\gamma_i^{(g)}(t)$ (Eq. 14):

$$\begin{aligned} \dot{\beta}_g(t) &= \mathbf{T}_v : (\sigma_g(t) - \bar{\sigma}(t)), \quad \forall g \in [1; N], \quad \beta_g(0) = 0 \\ \tau_i \dot{\gamma}_i^{(g)}(t) + \gamma_i^{(g)}(t) &= \mathbf{T}_i : (\sigma_g(t) - \bar{\sigma}(t)), \quad \forall i \in [1; N_c], \quad \forall g \in [1; N], \quad \gamma_i^{(g)}(0) = 0 \end{aligned} \quad (14)$$

3.4 Crystallographic and morphological texture

The various crystallographic phases that constitute the polycrystalline aggregate are taken into account in the model by a discrete crystallographic orientation file that contains the three Euler's angles and the corresponding volume fraction for each phase. The file used here contains 240 orientations representative of the crystallographic texture of zirconium alloy thin rolled tubes³¹. The $\{0002\}$ and $\{1\bar{2}10\}$ pole figures corresponding to the RXA Zy-4 are shown Fig. 1. As an indication, the corresponding Kearns factors are $f_x = 0.565$, $f_y = 0.359$ and $f_z = 0.076$, the last value being lower than the experimental one which is close to $f_z = 0.1$.

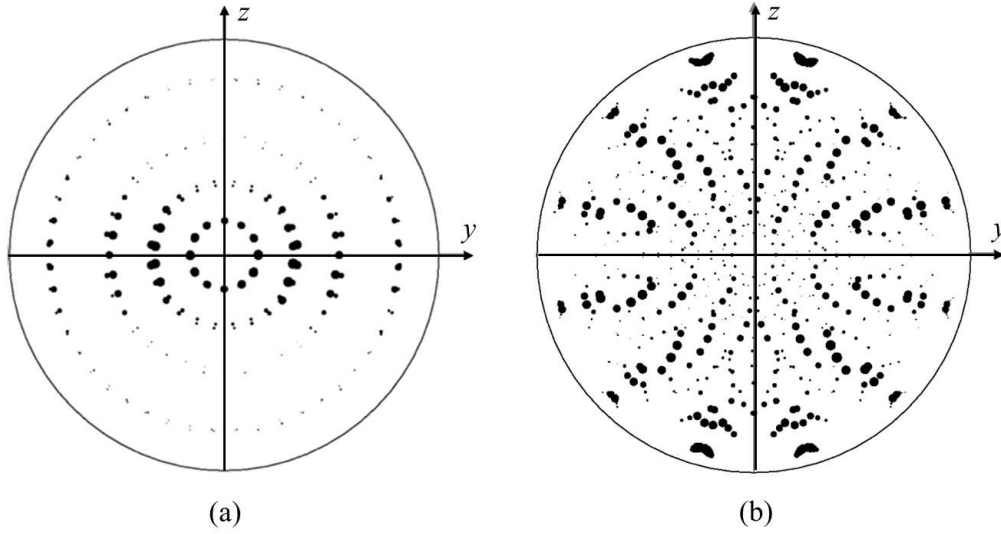


Figure 1: Discretized (a) $\{0002\}$ and (b) $\{1\bar{2}10\}$ pole figures representative of the texture of the RXA Zy-4.

The crystallographic textures of SRA and RXA Zy-4 are very similar. When comparing the two textures, the crystal is only rotated by an angle of 30° around the $\langle c \rangle$ axis. Because this rotation does not influence the transversely isotropic single crystal symmetry, the same texture file has been used.

The grain shape is taken into account in the modelling through the shape of the inclusion used in the self-consistent scheme. For RXA Zy-4, the inclusion is considered as a sphere with aspect parameters of the ellipsoid $a_1 = a_2 = a_3 = 1$.

Concerning SRA Zy-4, the inclusion is first considered as a sphere to separate the effect of the grain shape and the effect of the local behavior on the effective response of the polycrystal. Then, to highlight the effect of grain shape, an elongated ellipsoid is considered with the aspect ratio a_3 along the tube axial (z) direction set to 10 and the other two remaining equal to one. Simulations using these two shapes are reported in the following.

3.5 Implementation of the polycrystalline model in MFront

For a given time step, most mechanical solvers search the increment of displacement satisfying the equilibrium by an iterative process derived from the Newton-Raphson algorithm. At each equilibrium iteration, an estimation of the strain increment is computed by the current estimate of the displacement increment at each quadrature point. This strain increment is used to integrate over the time step the ordinary system of differential equations formed by the constitutive equations Eq. 12 and Eq. 14. This provides a new estimate of the internal state variables of the material $(\xi, \zeta_i, \eta_i^g, \beta^g, \gamma_i^g)$

at the end of the time step and a new estimate of the macroscopic stress $\bar{\sigma}$. This macroscopic stress is used to estimate whether equilibrium is satisfied. If this is not the case, a new estimate of the displacement increment is proposed.

In this work, the behaviour integration is performed using an explicit Runge-Kutta-Fehlberg³² scheme with automatic sub-stepping and is implemented using the opensource MFront code generator²². The implementation closely follows this document³³. The mechanical tests are simulated using the simulation tool, referred to as MTest, delivered with the opensource software MFront.

It is worth noting that the current implementation of the polycrystalline model does not provide the exact consistent tangent operator but only the effective elastic stiffness. This may lead to linear convergence of the equilibrium algorithm, unless acceleration algorithms are used, which is the case in the MTest simulations used in this work³⁴.

4. Local behavior, parametrization method and simulation results

4.1 Local behaviour

4.1.1 Elastic behavior

In this paper, all the tensors mentioned are written using Kelvin-Voigt notation³⁵. The local elastic behavior is characterized by the transversely anisotropic elastic compliance tensor ($\mathbf{M}_e^{(g)}$) or stiffness tensor ($\mathbf{C}^{(g)}$). The five independent coefficients of the local stiffness tensor at 350°C obtained from the work of Fisher and Renken³⁶ are given in the following: $C_{11} = 127800$ MPa, $C_{12} = 79300$ MPa, $C_{13} = 65800$ MPa, $C_{33} = 154300$ MPa, $C_{55} = C_{66} = 55200$ MPa, and $C_{44} = C_{11} - C_{12}$.

4.1.2 Irradiation creep behavior

The irradiation creep deformation mechanisms are still not well known⁴. In the case of zirconium alloys, it has often been considered that glide enhanced by climb can explain irradiation creep deformation³. However, several authors have also suggested that anisotropic diffusion of point defects under stress toward grain boundaries could explain irradiation creep deformation, at least for very small grains size³⁷. In this work, we have chosen to adopt the same approach as in the references^{10,12,13} which assumes that the irradiation creep is linear with stress. This can be justified by considering that irradiation creep is the result of dislocation glide assisted by climb where the rate limiting process is the point defect diffusion.

Due to the HCP symmetry of the crystallographic phases, the irradiation compliance tensor (\mathbf{M}_v) is transversely isotropic. The irradiation creep deformation being isochoric, only three independent coefficients (which are in fact eigenvalues of the tensor) are necessary to define it. This coefficients are noted (K_E, K_t, K_l) and correspond to $K_E = K_1$, $K_t = K_2$ and $K_l = K_3$ used by Tomé et al.¹⁰. Thanks to this approach, strong assumptions

on microscopic deformation processes are avoided. However, assuming transverse isotropy implies that the local behavior is only related to the crystal symmetry and that the shape of the grains (if it is not transversely isotropic) has no impact on the local behavior of the crystal.

The irradiation creep compliance tensor can then be written as a linear combination of orthogonal tensors as Eq. 15.

$$\mathbf{M}_v = K_E \mathbf{K}_E + K_t \mathbf{K}_t + K_l \mathbf{K}_l \quad (15)$$

These tensors are expressed in the crystal frame, with the third unit vector aligned with the <c> axis, as Eq. 16.

$$\mathbf{K}_E = \begin{pmatrix} \frac{1}{6} & \frac{1}{6} & -\frac{1}{3} & 0 & 0 & 0 \\ \frac{1}{6} & \frac{1}{6} & -\frac{1}{3} & 0 & 0 & 0 \\ -\frac{1}{3} & -\frac{1}{3} & \frac{2}{3} & 0 & 0 & 0 \\ 0 & 0 & 0 & 0 & 0 & 0 \\ 0 & 0 & 0 & 0 & 0 & 0 \\ 0 & 0 & 0 & 0 & 0 & 0 \end{pmatrix}$$

$$\mathbf{K}_t = \begin{pmatrix} \frac{1}{2} & -\frac{1}{2} & 0 & 0 & 0 & 0 \\ -\frac{1}{2} & \frac{1}{2} & 0 & 0 & 0 & 0 \\ 0 & 0 & 0 & 0 & 0 & 0 \\ 0 & 0 & 0 & 1 & 0 & 0 \\ 0 & 0 & 0 & 0 & 0 & 0 \\ 0 & 0 & 0 & 0 & 0 & 0 \end{pmatrix} \quad (16)$$

$$\mathbf{K}_l = \begin{pmatrix} 0 & 0 & 0 & 0 & 0 & 0 \\ 0 & 0 & 0 & 0 & 0 & 0 \\ 0 & 0 & 0 & 0 & 0 & 0 \\ 0 & 0 & 0 & 0 & 0 & 0 \\ 0 & 0 & 0 & 0 & 1 & 0 \\ 0 & 0 & 0 & 0 & 0 & 1 \end{pmatrix}$$

The sum of these tensors is equal to the isotropic projector K which extract the deviatoric part of a tensor. When applied to a given stress tensor σ , K_E returns a traceless tensor containing its axial component, whereas K_t and K_l extract respectively its transverse and longitudinal shear components.

4.1.3 Irradiation growth behavior

Previous studies^{38,39,40} have proven that the volume change of zirconium alloys under irradiation remains small, resulting in a very limited swelling under irradiation. Studies^{5,41} have also shown that the zirconium single-crystal exhibits a shortening along the <c> axis under irradiation and an expansion in the basal plane. As a result, the local growth strain is taken into account as an isochoric eigenstrain that increases linearly with time. Due to the HCP crystal's symmetry, this tensor is transversely isotropic. As a first step, a simple linear irradiation growth has been chosen for this model that is suitable for a low irradiation dose before growth breakaway. More complex approaches such as the one developed by Barashev et al.⁴² and Patra et al.⁴³ could be implemented in future works. The growth strain rate tensor is then expressed in the crystal frame as Eq. 17:

$$\dot{\varepsilon}_0^{(g)} = K_0 \begin{pmatrix} 1/2 & 0 & 0 \\ 0 & 1/2 & 0 \\ 0 & 0 & -1 \end{pmatrix} \quad (17)$$

The local constitutive behavior is thus characterized by only four adjustable material parameters: K_0 , K_E , K_t and K_l . These parameters have been identified for a fixed flux of $1.7 \times 10^{18} \text{ n.m}^{-2}.\text{s}^{-1}$. As a consequence, the dependence with neutron flux of local creep and growth behaviors does not appear explicitly in the formula.

4.2 Parametrization method

In this section we describe the procedure used to determine a set of four parameters (K_0 , K_E , K_t , K_l) to numerically reproduce the experiments presented earlier. Among the available experimental data, only the irradiation creep test conducted with an internal pressure equivalent to an applied hoop stress of 90 MPa has been retained for the fitting procedure. Unlike the other tests it was conducted during a longer period of time and allows a correct measurement of the steady state creep rate along both hoop and axial directions. The procedure is divided in three steps. In the first and second steps, irradiation creep and growth are identified separately. As a consequence, when considering creep behaviour, the growth parameter is set to zero. On the other hand, when considering growth, the macroscopic stress is set to zero, but not the local ones, allowing creep and relaxation to occur within the phases. Finally, with both irradiation creep and growth mechanisms active, the simulated macroscopic irradiation creep behavior is compared to the experiments and possibly slightly adjusted again to obtain the best fit of the experimental data.

4.2.1 Parametrization of irradiation creep anisotropy

During the irradiation internal pressure creep test conducted under a hoop stress of 90 MPa, the steady state is reached²⁷ for a fluence of about 3×10^{25} n.m⁻², which corresponds to 1.7×10^7 s for a neutron flux of 1.7×10^{18} n.m⁻².s⁻¹. As a consequence, the set of experimental points used to calculate the steady strain rate has been reduced by considering only the points above 1.5×10^5 s. Linear regressions have been performed for both irradiation creep and growth experimental curves and for both hoop and axial strains. Then, assuming additivity of the macroscopic creep and growth, the steady state creep rate alone is obtained by subtracting the growth rate from the total strain rate. The ratio (R_{exp}) between the steady state creep strain rate along the axial direction (z) with respect to the strain rate along the hoop direction (y) is then computed.

$$R_{exp} = \frac{\left(\frac{\dot{\epsilon}_{zz}^{creep}}{\dot{\epsilon}_{zz}}\right)_{exp}}{\left(\frac{\dot{\epsilon}_{yy}^{creep}}{\dot{\epsilon}_{yy}}\right)_{exp}} = \frac{\frac{\dot{\epsilon}_{zz} - \dot{\epsilon}_{zz}^{growth}}{\dot{\epsilon}_{zz}}}{\frac{\dot{\epsilon}_{yy} - \dot{\epsilon}_{yy}^{growth}}{\dot{\epsilon}_{yy}}} \quad (18)$$

In the considered numerical model, during the steady regime and in absence of growth, the macroscopic strain rate depends solely on the purely viscous effective creep compliance tensor \tilde{M}_v .

$$\dot{\bar{\epsilon}}(t) = \tilde{M}_v : \bar{\sigma}(t) \quad (19)$$

The ratio between the creep strain rates along the axial and hoop directions is computed and compared with the experiment. During an internal pressure test with closed ends, the macroscopic stress tensor applied is actually triaxial. For a thin tube ($\eta = e/D_m^{ini} = 0.067$) it has been shown by Onimus et al.²⁸ that a good approximation of this stress tensor (second order approximation) is given by Eq. 20:

$$\bar{\sigma} = \frac{PD_m^{ini}}{2e} \begin{pmatrix} -\eta & 0 & 0 \\ 0 & 1 - \eta & 0 \\ 0 & 0 & 1/2 - \eta \end{pmatrix} \quad (20)$$

This definition has been used in our simulations. Considering the stationary creep rate, the ratio between the strain rate along the axial direction and the strain rate along the hoop direction can be then expressed as Eq. 21:

$$R_{sim} = \frac{\left(\dot{\epsilon}_{zz}^{creep}\right)_{sim}}{\left(\dot{\epsilon}_{yy}^{creep}\right)_{sim}} = \frac{-\eta\tilde{M}_{v(xz)} + (1-\eta)\tilde{M}_{v(zy)} + \left(\frac{1}{2}-\eta\right)\tilde{M}_{v(zz)}}{-\eta\tilde{M}_{v(xy)} + (1-\eta)\tilde{M}_{v(yz)} + \left(\frac{1}{2}-\eta\right)\tilde{M}_{v(zy)}} \quad (21)$$

The relative error (E_1) between the simulated steady state strain rate ratio (R_{sim}) and the experimental steady state strain rate ratio (R_{exp}), defined as Eq. 22, has been computed for various couples (K_E/K_t , K_l/K_t) with constant K_t value. Because the irradiation creep compliance tensor is positive definite, only positive values for K_E , K_t and K_l are investigated. Adequate parameters are obtained for an error below 1%.

$$E_1 = \frac{|R_{sim} - R_{exp}|}{|R_{exp}|} \quad (22)$$

Simulations have been conducted for the RZA Zy-4 using aspect ratios for the inclusion equal to $a_1 = a_2 = a_3 = 1$. For SRA Zy-4, there are two types of inclusions: a spherical and an elongated with aspect ratios $a_1 = a_2 = 1$ and $a_3 = 10$.

The sets of optimal points (i.e. satisfying the criteria $E_1 < 1\%$) are displayed on Fig. 2 for both alloys using spherical and ellipsoidal shapes (in the SRA Zy-4 case). For the recrystallised alloy, parameters $\left(\frac{K_l}{K_t}, \frac{K_E}{K_t}\right)$ proposed in the literature^{12,13} are also shown.

One can notice that the optimal sets are not unique but are spread along a curve. The under-determination of optimum parameter sets is explained because in the experimental database, only internal pressure tests are available. Using numerical simulations, we have been able to check that knowing the behavior for axial creep tests would lead to the determination of a single couple of parameters. This shows that for modeling requirements it is important to know both the creep behavior for internal pressure and for axial tension creep tests.

It is interesting to note that the loci of adequate parameters are very different for the two materials. This results from their different anisotropic behaviour. As discussed further below, this can be interpreted in terms of differences in deformation mechanisms at the local scale.

Furthermore, it can be noticed that by changing the shape of the inclusion from sphere to elongated ellipsoid, the optimum parameter locus is slightly shifted towards higher $\frac{K_l}{K_t}$ values. The influence of the inclusion shape is investigated in the following.

All the points $\left(\frac{K_l}{K_t}, \frac{K_E}{K_t}\right)$ shown on the locus (2a, 2b) provide adequate steady state creep anisotropic behavior. However, depending on the parameters chosen, the transient behavior is different, for creep and growth. This has been explored by testing various

points from the optimum locus and comparing the predicted creep behavior with experimental data. Based on these simulations one adequate point on the locus has been selected for each material.

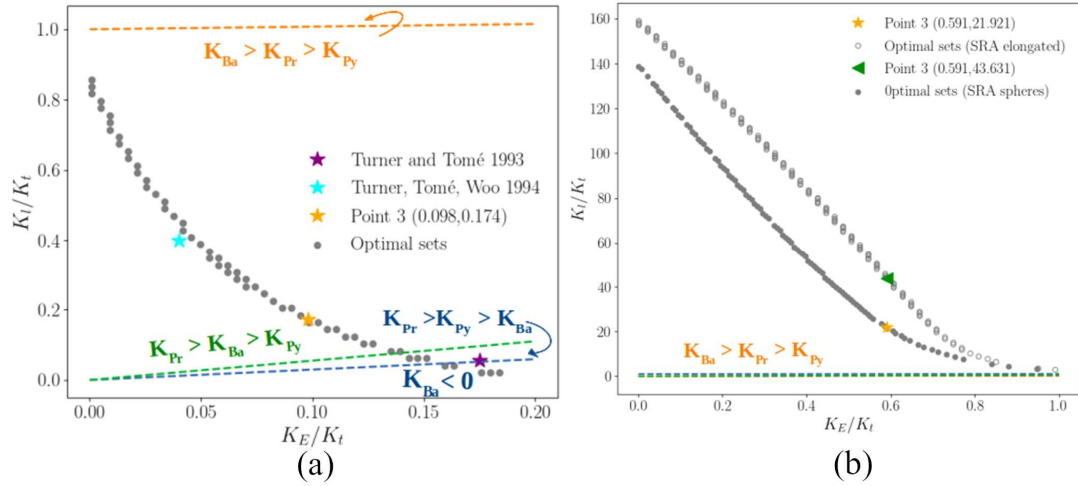


Figure 2: Representation of optimal points (i.e. $E_1 < 1\%$) for (a) RXA and (b) SRA Zr-4 alloys.

4.2.2 Parametrization of the magnitude of creep rate

Once suitable K_E/K_t and K_I/K_t ratios have been found, the parameter K_t can be determined from the steady state creep rate along the hoop direction (y). As done previously, the steady state irradiation creep rate is computed by subtracting the growth rate to the total strain rate. The steady state creep rate is then computed by the polycrystalline model and compared to the experiment. The parameter K_t is chosen such that the corresponding error, defined in Eq. 23, is below 1%.

$$E_2 = \frac{\left| \left(\dot{\bar{\epsilon}}_{yy}^{creep} \right)_{sim} - \left(\dot{\bar{\epsilon}}_{yy}^{creep} \right)_{exp} \right|}{\left| \left(\dot{\bar{\epsilon}}_{yy}^{creep} \right)_{exp} \right|} \quad (23)$$

4.2.3 Parametrization of the irradiation growth parameter

In this last step, the experimental growth tests are now considered. The steady state growth rate is simulated for various values for the parameter K_0 , and compared to the experimental steady state growth rate. The adequate value for the parameter K_0 is

obtained when the relative error between simulation and experiment, defined in Eq. 24, is below 1%.

$$E_3 = \frac{\left| \left(\frac{\dot{\epsilon}_{zz}^{growth}}{\epsilon_{zz}} \right)_{sim} - \left(\frac{\dot{\epsilon}_{zz}^{growth}}{\epsilon_{zz}} \right)_{exp} \right|}{\left| \left(\frac{\dot{\epsilon}_{zz}^{growth}}{\epsilon_{zz}} \right)_{exp} \right|} \quad (24)$$

4.3 Simulation results

The internal pressure creep test is finally simulated with the four parameters found previously. In that case, local irradiation growth also occurs simultaneously with local irradiation creep. The simulated behavior, for both internal pressure creep test and irradiation growth test is compared to the experiments on Fig. 3. The final chosen parameters for each case are given in Table 1.

Table 1: Sets of chosen parameters for the two materials.

	K_E (MPa ⁻¹ .s ⁻¹)	K_t (MPa ⁻¹ .s ⁻¹)	K_l (MPa ⁻¹ .s ⁻¹)	K_0 (s ⁻¹)
RXA Zy-4 spheres	9.41×10 ⁻¹³	9.6×10 ⁻¹²	1.67×10 ⁻¹²	3.55×10 ⁻¹¹
SRA Zy-4 (spheres)	1.68×10 ⁻¹²	2.85×10 ⁻¹²	6.25×10 ⁻¹¹	1.3×10 ⁻¹⁰
SRA Zy-4 (elongated ellipsoids)	9.6×10 ⁻¹³	1.62×10 ⁻¹²	7.07×10 ⁻¹¹	1.3×10 ⁻¹⁰

Concerning irradiation growth of RXA Zy-4 (3a), it can be seen that the steady state growth rate is well predicted, as expected. However, the model is not able to reproduce the small growth transient at the beginning of the irradiation. On the contrary, the model predicts a slightly slower growth rate at the beginning of irradiation although a local linear growth strain has been introduced. This is explained by the local creep or relaxation of the phases caused by the inter-phase stresses. Several parameter sets, corresponding to the optimum locus, have been tried to improve the transient of the growth strain, but none of them were able to give better agreement. The prediction of a more rapid transient growth rate at the beginning of irradiation would require modifying the local growth constitutive equations by introducing an evolution with irradiation dose. It can also be

noticed that although the strain along the y -direction has not been used for the optimization of the parameters, it is well predicted by the model.

Concerning the creep behavior of RXA Zy-4, it can be noticed that the steady state strain rate along both y and z directions are well predicted by the model (Fig. 3c). However, the primary creep is not predicted by the model.

The model, using both spheres or elongated ellipsoid, is able to nicely reproduce the growth behavior of the SRA Zy-4 along the z -direction (Fig. 3b). Along the y -direction, the model also predicts an adequate growth rate, considering the experimental uncertainty for this measurement. It is interesting to note that changing the inclusion from sphere to ellipsoid does not affect the growth behavior.

The steady state creep rates of SRA Zy-4 along the y and z direction are correctly reproduced, as expected (Fig. 3d). The model is able to predict a slight transient. This is due to the visco-elastic coupling that is taken into account thanks to the collocation method. However, it can be noticed that the transient predicted for the SRA Zy-4 is not as pronounced as in the experiments.

The fact that the creep transient cannot be correctly reproduced by the model proves that the primary creep cannot be attributed to the visco-elastic coupling but is due to the microstructure evolution at the beginning of irradiation. It must also be mentioned that the thermal creep, which is not taken into account here, could play a role in the primary creep. Its contribution in this regime could progressively decrease as the radiation damage builds up.

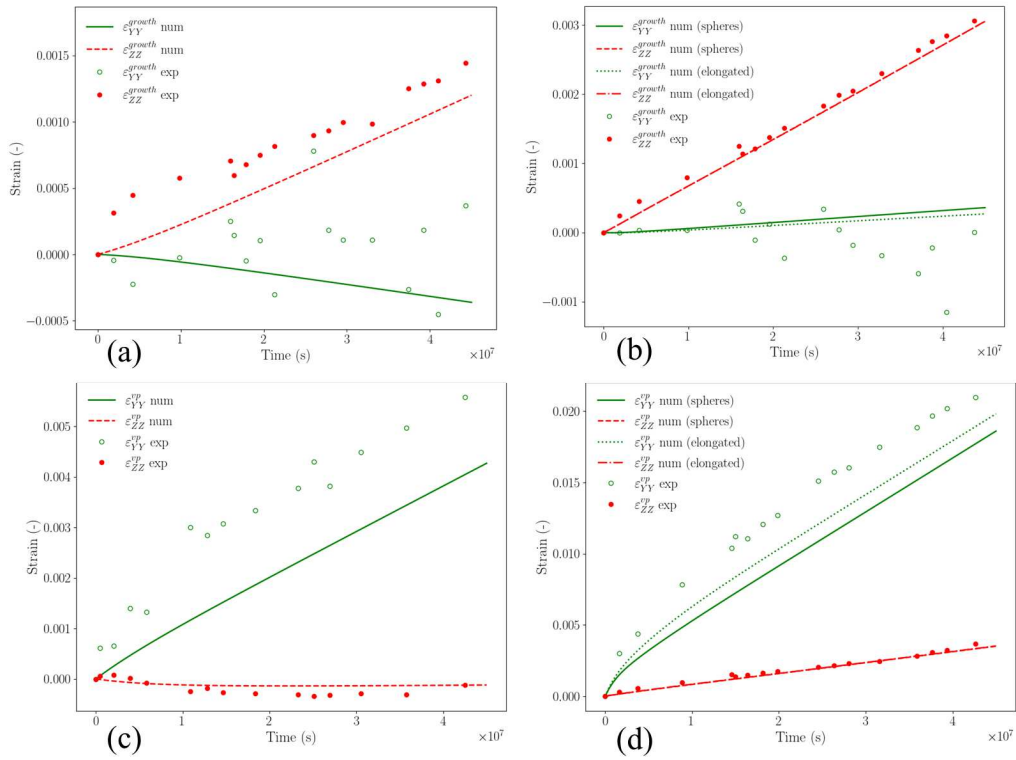


Figure 3: Simulations of (a), (b) irradiation induced growth and (c), (d) irradiation creep under internal pressure (90 MPa target hoop stress) and comparison with experiments, for RZA Zy-4 (3a,3c) and SRA Zy-4 (3b,3d) with either spherical (solid and dashed lines) and elongated (dotted lines) grain shape.

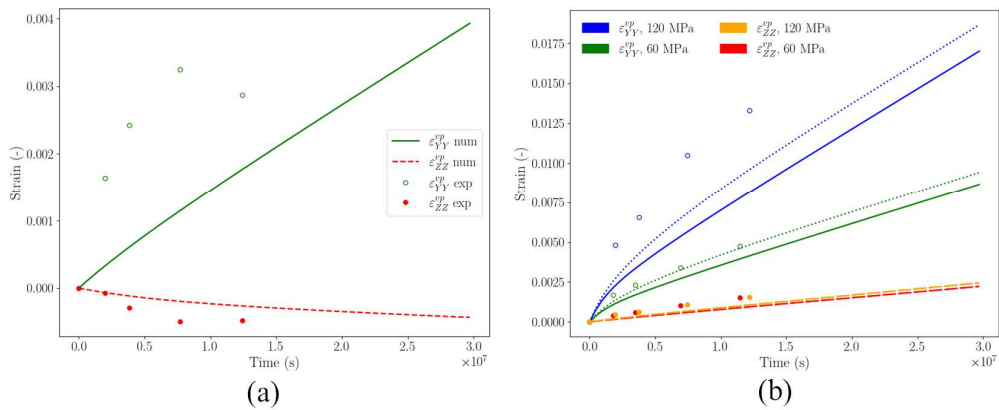


Figure 4: Simulations of irradiation creep under internal pressure for (a) RZA Zy-4 with 120 MPa target hoop stress, (b) SRA Zy-4 with 60 and 120 MPa target hoop stress (considering either spherical inclusions represented by solid lines or elongated ellipsoidal inclusions represented by dotted lines). The simulations are compared with experiments. In the axial direction the results coincide for both grain shapes.

The polycrystalline model has been used to compute the internal pressure creep tests conducted with lower or higher applied stresses.

It can be seen that for RXA Zy-4 and SRA Zy-4 under a hoop stress of 120 MPa, the model predicts a lower creep rate than in the experiment. This suggests that the stress exponent for irradiation creep is higher than 1. Concerning the creep test done on SRA Zy-4 under a hoop stress of 60 MPa, the prediction of the model is in good agreement with the experiment (Fig. 4b).

5. Discussion

5.1 Discussion on the influence of grain shape

Following the work done by Tomé et al.¹⁰, the influence of the shape of the inclusion used in the self-consistent model has been investigated.

This parameter aims at representing the shape of the crystalline grains of the considered material, at least from the self-consistent theory point of view. However, it must be kept in mind that it does not take into account the effect of grain boundaries on the deformation mechanisms such as dislocation motion or point defect diffusion. For this study, the growth term was set to zero. The ratio between the axial and hoop irradiation creep strain rate in the steady regime, referred to as R_{sim} and defined in Eq. 21, was then computed for various inclusion shapes.

First the parameters for the SRA Zy-4 obtained for spherical inclusions have been used. The optimum value for R_{sim} , the closest to R_{exp} , is obtained for $a_3 = 1$. Then the aspect ratio a_3 has been modified, from 1 up to 100, keeping $a_1 = a_2 = 1$ (Fig. 5). It is observed that the value R_{sim} decreases only slightly when the ellipsoid is elongated along the z -direction up to $a_3 = 5$. When the ellipsoid is further elongated the influence of the grain shape is very low. In a second step, the parameters for the SRA Zy-4 obtained for elongated ellipsoidal inclusions ($a_3 = 10$ and $a_1 = a_2 = 1$) have been used (see Table 1). In that case, the optimum value for R_{sim} , the closest to R_{exp} , is obtained for $a_3 = 10$. A curve, similar than the one obtained with the first parameter set is obtained (Fig. 5).

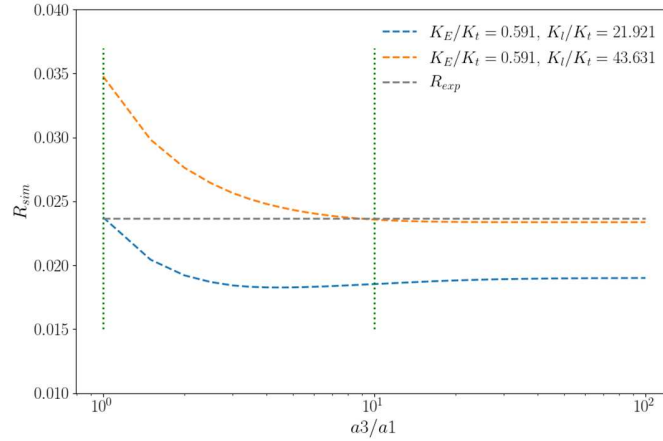


Figure 5: Evolution of the irradiation creep strain rate ratio with the shape of the phases.

5.2 Discussion on the irradiation creep deformation mechanisms

It can be noted that the macroscopic irradiation creep rate is always higher for the SRA Zy-4 than for the RXA Zy-4. This can also be seen at the local scale, when comparing the values of the coefficients K_E , K_t and K_l . The coefficient K_l is more than one order of magnitude higher for SRA Zy-4 than for the RXA Zy-4. This explains the higher creep rate during internal pressure creep tests. On the other hand, the coefficient K_E is similar for both alloys and the coefficient K_t is smaller for SRA Zy-4 than for RXA Zy-4. This higher creep rate for SRA Zy-4 could be due to the presence of a higher dislocation density than for RXA Zy-4. These numerous dislocations, with $\langle a \rangle$ and $\langle c+a \rangle$ Burgers vectors, can glide or climb, or both, under simultaneous irradiation and applied stress leading to a high strain rate. The elongated grains, in the axial direction, with small transverse dimensions for SRA Zy-4, especially the small sub-grains, could also induce a higher creep rate, as suggested by Walters et al.³⁷. The local anisotropic behavior is also significantly different between the two alloys. Again, this could be due to the difference in the dislocation microstructure and grain shape, or both.

It is difficult to analyze these differences more precisely without a clear idea of the active deformation mechanisms. Thanks to the tests conducted with various applied stresses (Fig. 4), it has been shown that the irradiation creep behavior is not exactly linear with stress, but seems to exhibit a stress exponent higher than 1. This suggests that the behavior is partly controlled by glide based mechanisms. Assuming that irradiation creep deformation of zirconium is explained by glide enhanced by climb^{2,4}, the anisotropic irradiation creep compliance tensor can be analyzed in terms of slip systems.

By assuming dislocation glide with a linear stress dependence, the creep compliance tensor \mathbf{M}_v can be expressed as a linear combination of the orientation tensors of the different slip systems (prismatic $\langle a \rangle$, basal $\langle a \rangle$ and pyramidal $\langle c+a \rangle$) (Eq. 25).

$$\mathbf{M}_v = K_{Pr} \sum_{i=1}^3 \mu_i^{Pr} \otimes \mu_i^{Pr} + K_{Ba} \sum_{i=1}^3 \mu_i^{Ba} \otimes \mu_i^{Ba} + K_{Py} \sum_{i=1}^{12} \mu_i^{Py} \otimes \mu_i^{Py} \quad (25)$$

with μ_i^\bullet the Schmid tensor of the i^{th} slip system of the \bullet family. The expression of the three eigenvalues of \mathbf{M}^v (K_l, K_t, K_E) as a function of the viscous compliances of the slip systems (K_{Ba}, K_{Pr}, K_{Py}) are given in Appendix. The ratios between the coefficients K_{Pr}/K_{Py} and K_{Pr}/K_{Ba} give the relative potential facility for the activation of the pyramidal and basal slip systems with respect to the prismatic. These ratios have been computed for several points of the locus of the optimum irradiation creep parameters. On the Fig. 2a and Fig. 2b several zones have been identified depending on the parameter values. In the case of RXA Zy-4, the prismatic slip is always more easily activated than the other slip systems. The pyramidal slip is the most difficult system to activate except for the small zone on the bottom right of the plot (between the blue and green dotted lines). Concerning the SRA Zy-4, the pyramidal slip is also the most difficult system to activate. However, for this material, it is the basal slip that is the easiest slip system to activate. This approach then suggests that under irradiation, basal slip is an easy slip system for SRA Zy-4 whereas it is the prismatic slip that is the easiest slip system for RXA Zy-4.

6. Application: monodimensional finite element simulation of a pipe using MTest

Following a similar approach as the one developed by Montgomery et al.¹⁵ and Patra and Tomé¹⁶, the polycrystalline model has been coupled to the pipe module of the MTest solver delivered with the opensource software MFront. This module allows the simulation of a 1D finite element calculation on pipes using the axisymmetrical generalized plain strain hypothesis classically used in mono-dimensional fuel performance codes⁴⁴. Only the three diagonal components of the stress and strain tensors are thus considered. The evolution of stresses and strains along the radius of the tube can be computed for simple tests or for complex non-monotonic loading. These simulations can be seen as a preliminary step towards the coupling of the polycrystalline model with fuel performance codes.

The finite element simulations of growth and internal pressure creep tests are compared with the material point simulations results presented above. The values of stresses and strains computed in the middle of the tube are in very good agreement with the values obtained for the material point simulations (1% relative discrepancy for radial and hoop strains and 1% relative discrepancy for hoop and axial stresses). Furthermore the mean hoop creep strain defined as Eq. 2 (approximated for small strains) is also computed. This mean hoop strain is 6% (relative discrepancy) below the value computed at the middle radius showing that this formula is an approximated estimation of the hoop strain at the middle radius of the tube.

Finally, the 1D finite element pipe module is used to compute a complex non-monotonic loading. The dimensions of the inner and outer radius are of 4.15 mm and 4.75 mm respectively. The mesh is constructed with five quadratic elements (3-node linear elements with quadratic shape function) along the thickness of the tube. An internal pressure of 0.7 MPa and an outer pressure of 15.5 MPa have been applied to the tube, mimicking the effect of the primary coolant and the inner pressure in the tube. In addition, a swelling perfectly rigid mandrel is introduced inside the tube. The initial radius of the mandrel is equal to 4.1 mm. The mandrel progressively swells (isotropic strain tensor) with a strain rate equal to 10^{-10} s^{-1} . This mandrel aims at mimicking the swelling of the pellet that occurs in-reactor. In this approach no thermal expansion and no densification of the pellet are taken into account.

Because the mean fast neutron flux considered for pressurized water reactor (PWR) equal to $9.18 \times 10^{17} \text{ n.m}^{-2}.\text{s}^{-1}$ is lower than the one used in the previous experiments ($1.7 \times 10^{18} \text{ n.m}^{-2}.\text{s}^{-1}$), the identified parameters (K_0 , K_E , K_t and K_l) have been multiplied by a factor equal to 0.54 for consistency with the typical PWR fast neutron flux. It must be noted that even if the simulation is not fully representative of in-reactor loading history it demonstrates the ability of the numerical tool to conduct complex finite element simulations with a polycrystalline model at each Gauss point. The simulations have been conducted for both RXA Zy-4 (with spheres) and SRA Zy-4 (with elongated ellipsoids). The results are shown on Fig. 6.

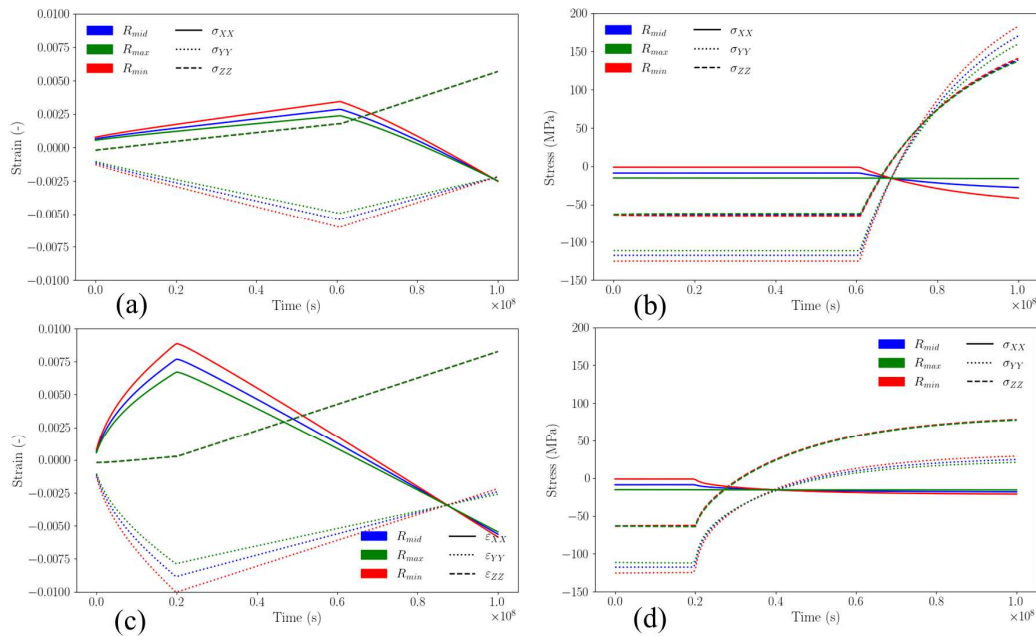


Figure 6: Macroscopic stress and strain responses to 1D Finite Element simulation of a complex loading for RXA Zy-4 (a,b) and SRA Zy-4 with elongated grains (c,d).

Figure 6a shows that for RXA Zy-4, the hoop strain starts to decrease due to unbalanced pressure conditions between the internal and external sides of the pipe. In the meantime, the axial strain increases because of both anisotropic creep and axial growth. At time $t=6.1 \times 10^7$ s the contact between the pipe and the mandrel occurs, resulting in an increase of both axial and hoop strains. The evolution of the stress components Fig. 6b shows a significant increase of the axial and hoop stress components when the contact is established.

For SRA Zy-4, the inward creep of the tube happens faster because of its higher creep rate (Fig. 6c). The contact with the mandrel thus occurs earlier (at $t = 2.0 \times 10^7$ s). From that point forward, both hoop and axial strains increase as well as hoop and axial stress reaching lower stress values than for RXA Zy-4 (Fig. 6d). This can be explained by the higher creep rate of the SRA Zy-4 that leads to a significant stress relaxation during the swelling of the mandrel.

It must be pointed out that because the model does not take into account non-linear thermal creep, the creep deformation is underestimated by the model especially considering the high stresses reached in the case of RXA Zy-4. In a future study, the model will be improved to be able to handle ageing non-linear elasto-visco-plastic behaviours, especially thermal creep, taking advantage of the internal variable formulation used¹⁸.

7. Conclusions

In this work, a self-consistent visco-elastic polycrystalline model has been developed to reproduce the in-reactor behaviour of fuel cladding tubes made of zirconium alloys, focusing on linear and non-aging irradiation creep and growth. An internal variable formulation of the polycrystalline model has been adopted and implemented in the MFront behaviour generation tool. This model is able to accurately describe the visco-elastic coupling occurring at the local scale. Thanks to both the chosen formulation and the numerical tool used, 1D Finite Element simulations have been performed on a pipe with complex non-monotonic loading. This is the first time that such a polycrystalline model has been coupled with Finite Element simulations.

An experimental database of in-reactor deformation for RXA and SRA Zy-4 has been analyzed. The anisotropic strain response during internal pressure creep tests and stress free growth tests has been used to determine the parameters of the local constitutive law. It is found that, for a given material, the parameters set is not unique. This brings to light that in order to fully determine the local behavior of the material under irradiation, additional mechanical tests are required (for instance, axial creep tests).

The origin of the irradiation creep transient has been studied by considering the visco-elastic coupling at the local scale. For the RXA Zy-4 alloy, it has been shown that the model does not correctly reproduce the pronounced transient regime. This study proves that the

transient response is not only due to the visco-elastic coupling occurring at the local scale but also results from microstructural evolutions under irradiation. For the SRA Zy-4 alloy, it has been observed that the morphological texture greatly influences the transient regime. Nevertheless, concerning the steady state creep, it has only a small effect on the creep anisotropy, when the representative inclusion is an elongated ellipsoid.

Concerning the deformation mechanisms, it has been assumed that irradiation creep deformation is due to dislocation glide enhanced by climb. With this assumption, the analysis of the anisotropic behavior shows that for RXA Zy-4, prismatic slip is easily activated whereas for SRA Zy-4 it is the basal slip that is the most easily activated slip system. The pyramidal $\langle c+a \rangle$ slip system is always the hardest slip system.

Finally, a complex non-monotonic loading, mimicking the in-reactor deformation of fuel rods, has been simulated. On one hand, the results showed that because of the rapid creep of SRA Zy-4, the contact between the clad and the pellet occurs early, but the stress level remains relatively low. On the other hand, for RXA Zy-4, the lower creep rate leads to a delayed contact between the pellet and the clad, but the stress level is significant. Further improvements of the polycrystalline model are required to be able to handle non-linear aging behaviours such as thermal creep.

Acknowledgments

This work has been funded by the project GAINÉ from the French nuclear tripartite institute CEA EDF Framatome. The authors want to thank A. Soniak for providing the experimental data base.

Appendix: Decomposition of the viscous compliance tensor M_v

By assuming that irradiation creep can be approximated by (linear) dislocation glide on slip systems, the viscous strain rate $\dot{\epsilon}^v$ reads (Eq. 26):

$$\dot{\epsilon}^v = \sum_s \dot{\gamma}^s \mu^s = \sum_s K^s (\mu^s : \sigma) \mu^s = \underbrace{\sum_s K^s (\mu^s \otimes \mu^s) : \sigma}_{M^v} \quad (26)$$

with μ^s the Schmid tensor of slip system (s). By considering prismatic, basal and pyramidal slip systems, the viscous compliance tensor can thus be written as Eq. 27 and Eq 28.

$$M_v = K_{Pr} \sum_{i=1}^3 \mu_i^{Pr} \otimes \mu_i^{Pr} + K_{Ba} \sum_{i=1}^3 \mu_i^{Ba} \otimes \mu_i^{Ba} + K_{Py} \sum_{i=1}^{12} \mu_i^{Py} \otimes \mu_i^{Py} \quad (27)$$

With

$$\begin{aligned} \sum_{i=1}^3 \mu_i^{Pr} \otimes \mu_i^{Pr} &= \frac{3}{4} K_t, \quad \sum_{i=1}^3 \mu_i^{Ba} \otimes \mu_i^{Ba} = \frac{3}{4} K_l \text{ and } \sum_{i=1}^{12} \mu_i^{Py} \otimes \mu_i^{Py} \\ &= p K_t + q K_l + \frac{9}{2} p K_E. \end{aligned} \quad (28)$$

The coefficients p and q are functions of the c/a ratio of the hexagonal close-packed structure following Eq. 29.

$$p = \frac{3(c/a)^2}{\left((c/a)^2 + \frac{3}{4}\right) \left((c/a)^2 + 1\right)} \text{ and } q = \frac{3 \left((c/a)^2 - \frac{3}{4} \right)^2 + \left(\frac{3}{4} \right)^2}{\left((c/a)^2 + \frac{3}{4} \right) \left((c/a)^2 + 1 \right)} \quad (29)$$

For zirconium crystalline structure, we have $c/a = 1.593$. Identification between relations Eq. 15 and Eq. 27 gives Eq/ 30.

$$K_l = \frac{3}{4} K_{Ba} + q K_{Py}, \quad K_t = \frac{3}{4} K_{Pr} + p K_{Py} \text{ and } K_E = \frac{9}{2} p K_{Py}. \quad (30)$$

It is remarked that, as the viscous compliances (K_{Ba}, K_{Py}, K_{Pr}) must be positive definite, the positive eigenvalues (K_E, K_l, K_t) must satisfy the following constraints (Eq. 31):

$$K_E/K_t < \frac{9}{2} \text{ and } K_l/K_t > \frac{2q}{9p} K_E/K_t \quad (31)$$

Furthermore, using Eq. 30, several domains can be determined.

In the case where $K_{Pr} > K_{Py}$

$$\frac{K_E}{K_t} < \frac{6p}{1 + \frac{4}{3}p} \quad (32)$$

If $K_{Ba} > K_{Py}$

$$\frac{K_l}{K_t} > \frac{2}{9} \left(\frac{3}{4} + q \right) \frac{1}{p} \frac{K_E}{K_t} \quad (33)$$

Finally, if $K_{Ba} > K_{Pr}$, then we have the following inequality :

$$\frac{K_l}{K_t} > \frac{2}{9} \left(\frac{q}{p} - 1 \right) \frac{K_E}{K_t} + 1 \quad (34)$$

References

1. D. G. Franklin, and R. B. Adamson. "Implications of Zircaloy Creep and Growth to Light Water Reactor Performance." *Journal of Nuclear Materials* 159 (1988): 12–21. [https://doi.org/10.1016/0022-3115\(88\)90082-7](https://doi.org/10.1016/0022-3115(88)90082-7).
2. R. B. Adamson, C. E. Coleman, and M. Griffiths, "Irradiation Creep and Growth of Zirconium Alloys: A Critical Review." *Journal of Nuclear Materials* 521 (2019): 167–244. <https://doi.org/10.1016/j.jnucmat.2019.04.021>.
3. F. Onimus, S. Doriot, and J.-L. Béchade. *Radiation Effects in Zirconium Alloys*. Comprehensive Nuclear Materials, Second Edition. Elsevier Ltd. Konings, R., Stoller, R. E. Eds. Vol. 3. (2020): 1-56. <http://dx.doi.org/10.1016/b978-0-12-803581-8.11759-x>.
4. F. Onimus, T. Jourdan, C. Xu, A. A. Campbell, and M. Griffiths. *Irradiation Creep in Materials*. Comprehensive Nuclear Materials, Second Edition. Elsevier Ltd. Konings, R., Stoller, R. E. Eds. Vol. 1 (2020): 310-366. <http://dx.doi.org/10.1016/b978-0-12-803581-8.11645-5>.
5. G. J. C., Carpenter, R. H. Zee, and A. Rogerson. "Irradiation Growth of Zirconium Single Crystals: A Review." *Journal of Nuclear Materials* 159 (1988): 86–100. [https://doi.org/10.1016/0022-3115\(88\)90087-6](https://doi.org/10.1016/0022-3115(88)90087-6).
6. M. Griffiths, "Irradiation Growth." In *Comprehensive Nuclear Materials, Second Edition*, Elsevier Ltd. Konings, R., Stoller, R. E. Eds, Vol. 1 (2020): 367–405.
7. N. Christodoulou, A. R. Causey, R. A. Holt, C. N. Tomé, N. Badie, R. J. Klassen, R. Sauvé, and C. H. Woo. "Modeling In-Reactor Deformation of Zr-2.5Nb Pressure Tubes in CANDU Power Reactors." *Zirconium in the Nuclear Industry: Eleventh International Symposium*, ASTM International, ASTM STP 1295 (1996): 518–537. <https://doi.org/10.1520/stp16188s>.
8. M. Limbäck, and T. Andersson. "A Model for Analysis of the Effect of Final Annealing on the In- and Out-of-Reactor Creep Behavior of Zircaloy Cladding." *Zirconium in the Nuclear Industry: Eleventh International Symposium* ASTM STP 1295 (1996): 448–468. <https://doi.org/10.1520/stp16185s>.
9. C. H. Woo "Polycrystalline Effects on Irradiation Creep and Growth in Textured Zirconium." *Journal of Nuclear Materials* 131, nos 2-3 (1985): 105–17. [https://doi.org/10.1016/0022-3115\(85\)90449-0](https://doi.org/10.1016/0022-3115(85)90449-0).
10. C. N. Tomé, C. B. So, and C. H. Woo. "Self-Consistent Calculation of Steady-State Creep and Growth in Textured Zirconium." *Philosophical Magazine A* 67, no 4 (1993): 917–30. <https://doi.org/10.1080/01418619308213968>.
11. R. A. Lebensohn, and C. N. Tomé. "A Self-Consistent Anisotropic Approach for the Simulation of Plastic Deformation and Texture Development of Polycrystals:

- Application to Zirconium Alloys.” *Acta Metallurgica Et Materialia* 41, no 9 (1993): 2611–24. [https://doi.org/10.1016/0956-7151\(93\)90130-k](https://doi.org/10.1016/0956-7151(93)90130-k).
12. P. A. Turner, and C. N. Tomé. “Self-Consistent Modeling of Visco-Elastic Polycrystals: Application to Irradiation Creep and Growth.” *Journal of the Mechanics and Physics of Solids* 41, no 7 (1993): 1191–211. [https://doi.org/10.1016/0022-5096\(93\)90090-3](https://doi.org/10.1016/0022-5096(93)90090-3).
 13. P. A. Turner, C. N. Tomé, and C. H. Woo. “Self-Consistent Modelling of Nonlinear Visco-Elastic Polycrystals: An Approximate Scheme.” *Philosophical Magazine A* 70, no 4 (1994): 689–711. <https://doi.org/10.1080/01418619408242256>.
 14. R. Brenner, J. L. Béchade, O. Castelnau, and B. Bacroix. “Thermal Creep of Zr–Nb1%–O Alloys: Experimental Analysis and Micromechanical Modelling.” *Journal of Nuclear Materials* 305, nos 2-3 (2002): 175–186. [https://doi.org/10.1016/s0022-3115\(02\)00923-6](https://doi.org/10.1016/s0022-3115(02)00923-6).
 15. R. Montgomery, C. Tomé, W. Liu, A. Alankar, G. Subramanian, and C. Stanek. “Use of Multiscale Zirconium Alloy Deformation Models in Nuclear Fuel Behavior Analysis.” *Journal of Computational Physics* 328 (2017): 278–300.
 16. A. Patra, and C. N. Tomé. “Finite Element Simulation of Gap Opening Between Cladding Tube and Spacer Grid in a Fuel Rod Assembly Using Crystallographic Models of Irradiation Growth and Creep.” *Nuclear Engineering and Design* 315 (2017): 155–69.
 17. F. Onimus, L. Gélébart, and R. Brenner. “Polycrystalline Simulations of in-Reactor Deformation of Recrystallized Zircaloy-4 Tubes: Fast Fourier Transform Computations and Mean-Field Self-Consistent Model.” *International Journal of Plasticity* 153 (2022): 103272.
 18. J.-M. Ricaud, and R. Masson. “Effective Properties of Linear Viscoelastic Heterogeneous Media: Internal Variables Formulation and Extension to Ageing Behaviours.” *International Journal of Solids and Structures* 46, nos 7-8 (2009): 1599–1606.
 19. Q. H. Vu, R. Brenner, O. Castelnau, H. Moulinec, and P. Suquet. “A Self-Consistent Estimate for Linear Viscoelastic Polycrystals with Internal Variables Inferred from the Collocation Method.” *Modelling and Simulation in Materials Science and Engineering* 20, no 2 (2012): 024003.
 20. R. Masson, M. E. B. Seck, J. Fauque, and M. Găărăjeu.. “A Modified Secant Formulation to Predict the Overall Behavior of Elasto-Viscoplastic Particulate Composites.” *Journal of the Mechanics and Physics of Solids* 137 (2020). <https://doi.org/10.1016/j.jmps.2020.103874>.
 21. P. A. Turner, C. N. Tomé, N. Christodoulou, and C. H. Woo. “A Self-Consistent Model for Polycrystals Undergoing Simultaneous Irradiation and Thermal Creep.”

- Philosophical Magazine A* 79, no 10 (1999): 2505–24.
<https://doi.org/10.1080/01418619908214296>.
22. T. Helfer, B. Michel, J.-M. Proix, M. Salvo, J. Sercombe, and M. Casella. “Introducing the Open-Source Mfront Code Generator: Application to Mechanical Behaviours and Material Knowledge Management Within the PLEIADES Fuel Element Modelling Platform.” *Computers & Mathematics with Applications* 70, no 5 (2015): 994–1023.
<https://doi.org/10.1016/j.camwa.2015.06.027>.
 23. R. Tewari, K. V. M. Krishna, S. Neogy, and C. Lemaignan.. “Zirconium and Its Alloys: Properties and Characteristics.” In *Comprehensive Nuclear Materials, Second Edition*, Elsevier Ltd., Konings, R., Stoller, R. E. Eds., Vol. 7 (2020): 284–302.
<http://dx.doi.org/10.1016/b978-0-12-803581-8.11735-7>.
 24. P. Delobelle, P. Robinet, P. Geyer, and P. Bouffieux. “A Model to Describe the Anisotropic Viscoplastic Behaviour of Zircaloy-4 Tubes.” *Journal of Nuclear Materials* 238 (2-3) (1996): 135–162.
 25. K. L. Murty, and I. Charit. “Texture Development and Anisotropic Deformation of Zircaloys.” *Progress in Nuclear Energy* 48, no 4 (2006): 325–59.
<https://doi.org/10.1016/j.pnucene.2005.09.011>.
 26. D. Gilbon, A. Soniak, S. Doriot, and J.-P. Mardon. “Irradiation Creep and Growth Behavior, and Microstructural Evolution of Advanced Zr-Base Alloys.” *Zirconium in the Nuclear Industry: Twelfth International Symposium* ASTM STP 1354 (2000): 51–73.
<https://doi.org/10.1520/stp14294s>.
 27. A. Soniak, N. L’Hullier, J.-P. Mardon, V. Rebeyrolle, P. Bouffieux, and C. Bernaudat. “Irradiation Creep Behavior of Zr-Base Alloys.” *Zirconium in the Nuclear Industry: Thirteenth International Symposium* ASTM STP 1423 (2002): 837–62.
<https://doi.org/10.1520/stp11419s>.
 28. F. Onimus, M. Bono, B. Verhaeghe, A. Soniak, and P. Pilvin. “Polycrystalline Modeling of the Behavior of Neutron-Irradiated Recrystallized Zirconium Alloys During Strain Path Change Tests.” *International Journal of Plasticity* 134 (2020): 102835.
<https://doi.org/10.1016/j.ijplas.2020.102835>.
 29. N. Gharbi, F. Onimus, D. Gilbon, J.-P. Mardon, and X. Feugas. “Impact of an Applied Stress on c-Component Loops Under Zr Ion Irradiation in Recrystallized Zircaloy-4 and M5.” *Journal of Nuclear Materials* 467 (2015): 785–801.
 30. R. A. Schapery. “Approximation Methods of Transform Inversion for Viscoelastic Stress Analysis.” *Proc Fourth USNat Congr Appl Mech*, 2 (1962): 1075.
 31. F. Onimus, M. Bono, J. Garnier, A. Soniak-Defresne, R. Limon, D. Gilbon, F. Bourlier, and A. Ambard. “Strain-Path Change Tests and Physically Based Polycrystalline

- Modeling of the Behavior of Recrystallized Zirconium Alloys.” In *Zirconium in the Nuclear Industry: 18th International Symposium* ASTM STP 1597 (2018): 180-213.
32. A. Fortin. « Analyse Numérique Pour Ingénieurs ». Presses internationales Polytechnique Ed (2011).
 33. F. Onimus, C. Gicquel, T. Helfer. “Explicit Integration of the Constitutive Equations of a Polycrystal Obtained by the Berveiller-Zaoui Homogenisation Scheme.” MFront documentation (2021), <https://thelfer.github.io/tfel/web/ExplicitBerveillerZaouiPolyCrystals.html>.
 34. I. Ramière, and T. Helfer. “Iterative Residual-Based Vector Methods to Accelerate Fixed Point Iterations.” *Computers & Mathematics with Applications* 70, no 9 (2015): 2210–26. <https://doi.org/10.1016/j.camwa.2015.08.025>.
 35. M. M. Mehrabadi, and S. C. Cowin. “Eigentensors of linear anisotropic elastic materials.” *The Quarterly Journal of Mechanics and Applied Mathematics* 43, no 1 (1990): 15–41. <https://doi.org/10.1093/qjmam/43.1.15>.
 36. E. S. Fisher, and C. J. Renken. “Single-Crystal Elastic Moduli and the Hcp→ Bcc Transformation in Ti, Zr, and Hf.” *Physical Review* 135, no 2A (1964): A482.
 37. L. Walters, G. Bickel, and M. Griffiths. “The Effects of Microstructure and Operating Conditions on Irradiation Creep of Zr-2.5 Nb Pressure Tubing.” In *Zirconium in the Nuclear Industry: 17th Volume*. ASTM STP 1543 (2015): 693-725.
 38. V. Fidleris, “The Irradiation Creep and Growth Phenomena.” *Journal of Nuclear Materials* 159 (1988): 22–42. [https://doi.org/10.1016/0022-3115\(88\)90083-9](https://doi.org/10.1016/0022-3115(88)90083-9).
 39. R. A. Holt, and A. R. Causey. “Volume Conservation During Irradiation Growth of Zr–2.5Nb.” *Journal of Nuclear Materials* 335, no 3 (2004): 529–533. <https://doi.org/10.1016/j.jnucmat.2004.07.042>.
 40. S. Yagnik, R. Adamson, G. Kobylansky, J.-H. Chen, D. Gilbon, S. Ishimoto, T. Fukuda, L. Hallstadius, A. Obukhov, and S. Mahmood. “Effect of Alloying Elements, Cold Work, and Hydrogen on the Irradiation-Induced Growth Behavior of Zirconium Alloy Variants.” *Zirconium in the Nuclear Industry: 18th International Symposium* ASTM STP 1597 (2018): 748–95. <https://doi.org/10.1520/stp159720160040>.
 41. G. J. C. Carpenter, R. A. Murgatroyd, A. Rogerson, and J. F. Watters. “Irradiation Growth of Zirconium Single Crystals.” *Journal of Nuclear Materials* 101, nos 1-2 (1981): 28–37. [https://doi.org/10.1016/0022-3115\(81\)90441-4](https://doi.org/10.1016/0022-3115(81)90441-4).
 42. A. V. Barashev, S. I. Golubov, and R. E. Stoller. “Theoretical Investigation of Microstructure Evolution and Deformation of Zirconium Under Neutron Irradiation.” *Journal of Nuclear Materials* 461 (2015): 85–94.

43. A. Patra, C. N. Tomé, and S. I. Golubov. "Crystal Plasticity Modeling of Irradiation Growth in Zircaloy-2." *Philosophical Magazine* 97, no 23 (2017): 2018–51. <https://doi.org/10.1080/14786435.2017.1324648>.
44. B. Michel, I. Ramière, I. Viillard, C. Introini, M. Lainet, N. Chauvin, V. Marelle, et al.. "Chapter 9 - Two Fuel Performance Codes of the PLEIADES Platform: ALCYONE and GERMINAL." In *Nuclear Power Plant Design and Analysis Codes*, edited by J. Wang, X. Li, C. Allison, and J. Hohorst, (2021) : 207–233. Woodhead Publishing Series in Energy. Woodhead Publishing. <https://doi.org/https://doi.org/10.1016/B978-0-12-818190-4.00009-7>.